

## Accepted Manuscript

Spectral two-dimensional inversion of frequency-domain induced polarisation data from a mining slag heap

Thomas Günther, Tina Martin

PII: S0926-9851(16)30009-X  
DOI: doi: [10.1016/j.jappgeo.2016.01.008](https://doi.org/10.1016/j.jappgeo.2016.01.008)  
Reference: APPGEO 2894

To appear in: *Journal of Applied Geophysics*

Received date: 30 April 2015  
Revised date: 7 December 2015  
Accepted date: 15 January 2016



Please cite this article as: Günther, Thomas, Martin, Tina, Spectral two-dimensional inversion of frequency-domain induced polarisation data from a mining slag heap, *Journal of Applied Geophysics* (2016), doi: [10.1016/j.jappgeo.2016.01.008](https://doi.org/10.1016/j.jappgeo.2016.01.008)

This is a PDF file of an unedited manuscript that has been accepted for publication. As a service to our customers we are providing this early version of the manuscript. The manuscript will undergo copyediting, typesetting, and review of the resulting proof before it is published in its final form. Please note that during the production process errors may be discovered which could affect the content, and all legal disclaimers that apply to the journal pertain.

# Spectral two-dimensional inversion of frequency-domain induced polarisation data from a mining slag heap

Thomas Günther<sup>a,\*</sup>, Tina Martin<sup>b</sup>

<sup>a</sup>*Leibniz Institute for Applied Geophysics, Hannover, Germany*

<sup>b</sup>*Federal Institute for Geosciences and Resources, Berlin, Germany*

---

## Abstract

Abandoned mining waste dumps may become potential resources for mineral reuse. For evaluating such structures, their spatial extension, the mineral content and predominating grain size needs to be determined. Amongst geophysical prospection methods, induced polarization (IP) is particularly suited since ore minerals show significant polarization characteristics. From laboratory measurements it is known that there is a relation between mineral concentration and chargeability, whereas the frequency content is mainly dominated by grain size.

Spectral IP (SIP) field data using a range of measuring frequencies can potentially map these quantities spatially. Instead of inverting the individual frequencies independently, we introduce a scheme where adjacent frequencies are constrained to each other. We test it using a synthetic model based on the Cole-Cole model with a body containing two parts of differing time constants. The inversion approach is able to reliably recover the Cole-Cole parameters.

---

\*Thomas.Guenther@liag-hannover.de

We apply the method to a field data set from a slag dump containing melting residuals from different minerals. The resulting models exhibit distinct zones of decreased conductivity and increased polarization that are not fully coincident. Furthermore, we observe a significant change in the spectral content. Taking into account recent laboratory investigations, the obtained chargeabilities hint to the occurrence of sufficient mineral concentration. In comparison with direct current resistivity, there is a clear benefit from using SIP field data in general and spectral analysis in particular.

---

## 1. Introduction

Historical mining waste dumps find themselves more and more in the focus for economy recovery. From the Middle Ages the western Harz Mountains in Germany represented an active mining area. Target were mainly lead (Pb), copper (Cu), silver (Ag) and later zinc (Zn) minerals (Poggendorf et al., 2015). Due to the former local mining conditions the waste dumps are often of small extent (typically lower than 200 m x 200 m). As most of the active waste dumps were closed many years ago, exact information about materials and processes is hard to obtain. It is assumed that the abandoned mining waste dumps have still a big potential for the supply of raw materials regarding a possible metal reprocessing. For the geophysical exploration of such mining dumps many different methods can be used, but originally the method of the induced polarisation (IP) is especially useful due to its sensitivity to metallic ingredients (Van Voorhis et al., 1973; Pelton et al., 1978b).

IP surveying is still one of the main exploration methods for minerals as it

can be deployed fast and cheap with large dipole transmitters and receivers. Traditionally, a 50% duty-cycle signal is injected and the decay that exhibits the polarization properties of the subsurface is registered as a time series. In many cases, the total chargeability is sufficient for mapping, however, increasingly analysis of separate time windows is done for gaining spectral information. IP measurements have been used for other targets such as waste site characterization (e.g., Fiandaca et al., 2013), environmental investigations (e.g., Slater & Lesmes, 2002) or contaminant imaging (e.g., Orozco et al., 2012a). Kemna et al. (2012) gives a recent overview of applications and methods.

Whereas time-domain IP (TDIP) has been traditionally used in the field, frequency-domain IP (FDIP) measurements are usually done in the laboratory as it is possible to cover a wide range of frequencies. Theoretically, FDIP and TDIP are two different ways of estimating the same properties. In field applications, FDIP takes more time because the frequencies are measured subsequently, whereas in TDIP the whole decay curve (typically from 30 ms to 3 s) bears the spectrum. However this might go along with decreased accuracy. Data acquisition at very low frequencies (1-10 mHz) requires long measurement time. To the contrary, TDIP is restricted to frequencies  $\leq 100$  Hz due to ramp length and time gates of the instruments. Up to now, no rigorous comparison between TDIP and FDIP has been presented. There have been a number of FDIP applications in the field of lithological characterization (e.g. Attwa et al., 2011), tree tomography (e.g. Martin & Günther, 2013) or prediction of hydraulic conductivity (e.g. Hördt et al., 2007).

In the field, the cable layout leads to electromagnetic coupling at higher frequencies which can limit the usable frequency range. These coupling effects depend on conductivity of the measured underground, measurement layout, geometric factor etc. and affect frequencies  $\geq 100$  Hz. Following the approach of Pelton et al. (1978b) for laboratory data, Kemna (2000) suggested to fit the apparent resistivity data with additional Cole-Cole terms for EM effects. Routh & Oldenburg (2001) proposed modelling of the EM coupling based on the conductivity obtained for the lowest frequency. Ingeman-Nielsen & Baumgartner (2006) demonstrated how these effects can be computed in case of known conductivity. However, in general cases with topography and real 2D structures this requires extensive effort. Schmutz et al. (2014) show that instruments with optic cables can decrease coupling and propose the use of the Schlumberger array with rectangular layout for soundings. For 2D measurements, Dahlin & Leroux (2012) proposed to use separated current and potential cables as this minimized coupling.

Development of 2D/3D modelling and inversion techniques started already in the 1970ies (Coggon, 1973; Pelton et al., 1978a). Inversion schemes were restricted to total chargeability, often with linearised approaches for the IP term (Oldenburg & Li, 1994; Beard et al., 1996) resulting in a two-step inversion approach. Oldenburg & Li (1994) proposed three different methods for estimating chargeability and found little difference for small polarizability. Kemna (2000) proposed a fully complex approach for single frequencies, however as well in two steps, of which the latter only inverts for the phase. He fitted Cole-Cole models for the individual model cells to retrieve spec-

tral characteristics. He found the time constant being well resolved, but the chargeability being highly correlated to the relaxation exponent. Routh et al. (1998) introduced a concept of retrieving Cole-Cole parameters directly through inversion, however only for synthetic data. Loke et al. (2006) proposed a step-wise approach where first initial resistivity and chargeability models are retrieved before Cole-Cole parameters are determined using Routh's method. In TDIP, spectral parameters were achieved by inverting each time gate and fitting a Cole-Cole models for each cell (Yuval & Oldenburg, 1997; Höning & Tezkan, 2007). Recently, Fiandaca et al. (2013) inverted time-domain data directly for Cole-Cole parameters.

Nevertheless, publications about spectral field data inversions remained extremely rare. Problems could be the availability of appropriate codes, the additional time spent on EM coupling in the frequency of interest (e.g., Kemna et al., 2012, and references therein). In some cases the subsurface is sufficiently described by single-frequency phase or total chargeability, in other cases the spectral behaviour is more complex than Cole-Cole.

There is very few literature on field IP on slag heaps or mining tailings: Yuval & Oldenburg (1996) estimated sulphide concentration from total chargeability, however only through borehole calibration. Ullrich et al. (2008) reported lab measurements on Cu-ore slag heaps showing broad phase spectra with maximum values of almost 200 mrad at a frequency of 1 Hz. They were able to delineate a slag heap using a 3D inversion of 2D FDIP profile measurements and deduced the quantity of slag material. Florsch et al. (2011) compared IP measurements in both FD and TD on a slag heap. By calibrating mass

↑ 3-1

concentration to partial chargeability with in the laboratory they described how total slag mass or volume could be derived, which was eventually done by Florsch et al. (2012) based on a 3D inversion of 2D profiles. However, their estimation of mineral content relies on the assumption of constancy, which was substantiated by Florsch et al. (2011). Using similar investigations as Pelton et al. (1978b), Hupfer et al. (in press) very recently demonstrated that both mineral content and grain size can be derived from the SIP chargeability and time constant.

In this study we want to investigate how these parameters can be obtained in field applications using appropriate inversion algorithms. After presenting the algorithms and example raw data, we demonstrate the applicability of the approach by using synthetic data from a well-defined model. Finally the field data are inverted and characteristic material properties are derived.

## 2. Material and methods

### 2.1. Spectral induced polarization

In TDIP the polarisation is quantified by the chargeability, i.e. the ratio of the potential  $U_s$  after turning off the supply current and the peak voltage  $U_p$  during current injection

$$m = \frac{U_s}{U_p} \quad (1)$$

In FDIP, one can describe polarization by the frequency effect ( $FE$ )

$$FE = \frac{\rho_0 - \rho_\infty}{\rho_\infty} \quad (2)$$

with  $\rho_0$  and  $\rho_\infty$  being the resistivities for a low frequency (DC) and for a high frequency (AC) measurement, respectively.  $m$  can be derived from  $FE$  using the relation

$$m = \frac{FE}{FE + 1} = \frac{\rho_0 - \rho_\infty}{\rho_0} . \quad (3)$$

To measure the spectral IP effect it is necessary to register amplitude  $|\rho|$  [ $\Omega\text{m}$ ] and phase  $\varphi$  [rad] of the complex resistivity (CR)  $\rho^*$  over a wide frequency range (usually between 1 mHz and several kHz). The complex resistivity  $\rho^*$  is linked to the measured quantities by

$$\rho^* = |\rho|e^{i\varphi} = \rho' + i\rho'' , \quad (4)$$

with  $\rho'$  and  $\rho''$  being the real and imaginary part of the complex resistivity, respectively and  $i=\sqrt{-1}$  is the imaginary unit. The real part describes the ohmic part (energy loss), whereas the imaginary part is related to the energy storage (polarization). Results can also be presented in terms of the complex conductivity  $\sigma^*$  ( $\sigma^* = 1/\rho^*$ ). Based on a parallel circuit, it can be described by a simple electric model (Marshall & Madden, 1959; Waxman & Smits, 1968). For low frequencies ( $f \ll 1000\text{ Hz}$ ) the conductivity can than



be expressed by

$$\sigma^* = \sigma_{\text{el}} + \sigma_{\text{surf}}^*(\omega) = [\sigma_{\text{el}} + \sigma'_{\text{surf}}(\omega)] + i\sigma''_{\text{surf}}(\omega), \quad (5)$$

with  $\sigma_{\text{el}}$  being the frequency-independent, electrolytic conductivity of the connected pore space,  $\sigma'_{\text{surf}}$  and  $\sigma''_{\text{surf}}$  are the frequency-dependent real and imaginary parts of the complex surface conductivity  $\sigma_{\text{surf}}^*$ , respectively (Lesmes & Frye, 2001). After (5), the imaginary part of the conductivity is only caused by surface conductivity, while the real part is affected by both electrolytic and surface conductivity (Slater & Lesmes, 2002; Kemna et al., 2004). For small polarization effects, the phase shift in the same model is given by

$$\varphi(\omega) \cong \frac{\sigma''_{\text{surf}}(\omega)}{\sigma_{\text{el}} + \sigma'_{\text{surf}}(\omega)} \cong \frac{\sigma''_{\text{surf}}(\omega)}{\sigma_{\text{el}}(\omega)} \quad (6)$$

with the assumption of a much higher electrolytic conductivity compared to surface conductivity ( $\sigma_{\text{el}} \gg \sigma'_{\text{surf}}(\omega)$ ) and a constant electrolytic conductivity for all measured frequencies.

The widely used Cole-Cole model (Pelton et al., 1978b) describes the complex resistivity by four parameters: the magnitude  $\rho$ , the chargeability  $m$ , the time constant  $\tau$  and the relaxation exponent  $c$ :

$$\rho^* = \rho \left[ 1 - m \left( 1 - \frac{1}{1 + (i\omega\tau)^c} \right) \right]. \quad (7)$$

Although only being a phenomenologic model originally given for dielectric permittivity, it is able to describe many materials with a limited number of

unknowns. However, the subsurface cannot be generally assumed to follow a Cole-Cole behaviour. Florsch et al. (2014) presented a much more general way to describe a medium by a combination of terms (7) with either  $c=1$  (Debye model) or  $c=0.5$  (Warbug model).

↑ 3-2

$$\rho^* = \rho \left[ 1 - \sum_k m_k \left( 1 - \frac{1}{1 + (i\omega\tau_k)^c} \right) \right]. \quad (8)$$

In both (7) and (8) the spectra exhibit a certain smoothness along frequency which can be considered in inversion.

## 2.2. Modelling and Inversion

We make use of the free and open-source code BERT (Günther & Rücker, 2005-2015). For the forward calculation, we use Finite Element analysis on irregularly discretized triangular meshes (Rücker et al., 2006; Rücker, 2011) for single frequencies, based on complex calculus. Wavenumber integration is done using a combination of Gauss-Legendre and Gauss-Laguerre nodes Kemna (2000). Inversion is also done on irregular triangles following the scheme described by Günther et al. (2006) and Rücker (2011). All inversion and fitting calculus is done within the Python framework pyGIMLi (Rücker & Günther, 2010-2015). Mesh generation is done using the mesh generator Triangle (Shewchuk, 1996) that allows to achieve a resolution-depending discretization of the subsurface. At the surface, element sizes are about a factor 3 below the electrode spacing, whereas they grow towards the bottom. The same mesh is used for all frequencies.

### Individual inversion

A single frequency inversion is done with a smoothness-constrained Gauss-Newton approach solver (Günther et al., 2006). The objective function to be minimized consists of  $L_2$ -norms of the misfits between data  $d_i$  and forward response  $f_i$ , weighted by their errors  $\epsilon_i$ , and a global roughness of first order:

$$\begin{aligned} \Phi_d + \lambda \Phi_m = & \sum_{i=0}^N \left( \frac{d_i - f_i(\mathbf{m})}{\epsilon_i} \right)^2 + \lambda \sum_{i=1}^B (m_i^{\text{left}} - m_i^{\text{right}})^2 \\ = & \|\mathbf{D}(\mathbf{d} - \mathbf{f}(\mathbf{m}))\|_2^2 + \lambda \|\mathbf{C}\mathbf{m}\|_2^2 \rightarrow \min \end{aligned} \quad (9)$$

The data vector  $\mathbf{d}$  holds the logarithms of the apparent resistivities (and  $\mathbf{f}$  accordingly), the model vector  $\mathbf{m}$  holds the logarithms of the cell resistivities. The regularization parameter  $\lambda$  weights the two norms and is a trade-off between data fit and model roughness. The latter is set up such that the data are fitted within the given noise level. To estimate noise from field data, reciprocal analyses can be done for resistivity (Udphuay et al., 2011) and phase (Orozco et al., 2012b) resulting in a relative and absolute error. As in our case no reciprocal data were available we used the standard values, i.e. 3% plus 100  $\mu\text{V}$  and 1% plus 3 mrad for resistivity and phase, respectively. In every inversion step we solve the system of normal equations for the model update  $\Delta\mathbf{m}$ :

$$(\mathbf{J}^T \mathbf{D}^T \mathbf{D} \mathbf{J} + \lambda \mathbf{C}^T \mathbf{C}) \Delta\mathbf{m} = \mathbf{J}^T \mathbf{D}^T \mathbf{D}(\mathbf{d} - \mathbf{f}(\mathbf{m}^k)) - \lambda \mathbf{C}^T \mathbf{C} \mathbf{m}^k \quad (10)$$

The Jacobian matrix  $\mathbf{J}$  contains the partial derivatives of the forward response with respect to the model parameters ( $J_{ij} = \partial d_i / \partial m_j$ ). The equation system is solved using a conjugate gradient solver (Günther et al., 2006), i.e. without explicitly forming the Hessian matrix.

One could directly invert for complex-valued resistivity. However, Kemna (2000) already pointed out problems originating in the fact that the real part is much larger than the imaginary part and this leads to inaccuracies for the latter. In the inversion software IP4DI, Karaoulis et al. (2013a) also follow this two-step approach, where first the resistivity amplitude is inverted and then the imaginary resistivity is independently fitted. Following Martin & Günther (2013), we make use of the symmetry of the complex Jacobian entries, i.e.  $\frac{\partial \rho_a'}{\partial \rho'} = \frac{\partial \rho_a''}{\partial \rho''}$  and initially approximate the real part with the amplitude. Equation (10) is then solved with  $\mathbf{m}$  and  $\mathbf{d}$  holding the imaginary (apparent) resistivity. The procedure is carried out for every frequency independently and referred to as individual inversion.

### *Simultaneous inversion*

Inversion results are prone to ambiguity and lead to artifacts that are hard to control. As a result, independent inversions show jumps along the frequency axis. However, even without assuming Cole-Cole behaviour, the frequency spectrum of subsurface parameters is expected to be smooth since the contributing relaxations have maximum  $c$  of 0.5 (Warburg model) and usually a distribution of grain sizes is present. Therefore we constrain neighbouring frequencies to each other. This could be done by starting at low frequencies

and using the model as a starting or reference model for the next higher frequency. However, the choice of the initial model is important. Furthermore, the different regularisation (smoothness of the model or the model difference) leads to different characteristics for the first model compared to the other. Therefore our approach is a simultaneous inversion as it was introduced for time-lapse ERT (Kim et al., 2009; Karaoulis et al., 2013b). All data are inverted simultaneously with smoothness constraints between adjacent model cells of the same frequency but also between identical model cells for adjacent frequencies. The model itself can be represented as a triangle prism mesh, each of the layers representing a frequency. This defines also the smoothness operator  $\mathbf{C}$ . The model vector  $\mathbf{m}$  subsidises the single-frequency model vectors  $\mathbf{m}^i$ , i.e.  $\mathbf{m} = [\mathbf{m}^1, \dots, \mathbf{m}^F]$ , where  $F$  is the number of frequencies. The same holds for the data vector, i.e.  $\mathbf{d} = [\mathbf{d}^1, \dots, \mathbf{d}^F]$ . As a result, the inverse problem is described by the block-diagonal Jacobian matrix

$$\mathbf{J} = \begin{bmatrix} \mathbf{J}^1 & 0 & \dots & 0 \\ 0 & \mathbf{J}^2 & \dots & 0 \\ \vdots & \vdots & \ddots & \vdots \\ 0 & 0 & \dots & \mathbf{J}^F \end{bmatrix}, \quad (11)$$

which can become very large ( $F \cdot D \times F \cdot M$ ). As  $D$  is in the order of 1000 and  $M$  even above, a value of  $F=16$  easily demands a memory size of about 4 GB. However, only a limited number of entries is actually nonzero making sparse matrices interesting. In this implementation we use a block matrix that stores only the individual Jacobian matrices  $\mathbf{J}^i$ . The routine solving

the normal equations (10) requires only multiplications from both sides with a vector, which is achieved by slicing the vectors. This makes the whole algorithm very fast and memory-efficient. It can be easily extended to 3D problems as the matrix size goes only with  $F$  and not  $F^2$ . For example, a data set of 10,000 data and 30,000 model cells requires 36 GB of memory instead of 600.

Here, the simultaneous inversion is first applied to the dc (amplitude) resistivity problem and then to the imaginary resistivity improvement. It could also be used for a fully complex inversion. Inversion stops if either the chi-square value goes below 1.0, if no improvement of the objective function can be achieved, or if a maximum iteration number (20).

↑ 3-4

### *2.3. Survey area and measurement details*

Several 2D SIP profiles were conducted at various mining dump heaps in Germany. We present data from a slag heap in the western Harz Mountains. Starting in the middle ages, copper, lead, silver and zinc ores were mined at different periods before it was abandoned more than 200 years ago. As a result, these dumps exhibit heterogeneous structures, i.e. variations in mineral composition and content, but also dominant grain size are expected. The total extension of the heap is about 600 m x 200 m but probably not continuous. Figure 1 shows the field layout for one of the profiles with the SIP256C instrument. In the background, slag material is found at the surface, whereas on other places a soil layer covers the heap.

[Figure 1 about here.]

The profiles were measured with the SIP256C instrument (Radic, 2004). The multi-channel, PC-controlled equipment records voltages for a current injection at different remote units in parallel. Although generally all array types would be possible, we used the dipole-dipole array as it diminishes cable coupling since optical fibre cables are used for transferring the time series to the base unit. Often, impolarisable electrodes are recommended for measuring small IP effects Kemna et al. (2012). We used standard stainless steel electrodes because of the expected high polarisation effects. Nevertheless we tried to minimize the electrode influence by using two electrodes at each measuring point; one for current injection (C), another for potential measurement (P). For the discussed profile, we used 41 electrodes with a distance of 1 m. Both electrodes (C/P) were put a few cm into the ground such that sufficient coupling to the ground was realised, at a distance of 10 cm (s. Fig. 1).

We made spectral measurements using a number of 14 frequencies: 1000, 500, 266, 125, 80, 40, 20, 10, 5, 2.5, 1.25, 0.625, 0.312, and 0.156 Hz. First, current was injected into all possible dipoles from adjacent electrodes and voltages were simultaneously recorded by all other unit dipoles. The geometric factor increases with  $n^3$ , where  $n$  is the separation factor between current and potential dipoles. This leads to bad signal-to-noise ratios for large  $n$  that needs to be accounted for by appropriate error estimates. To improve resolution for deeper model parts we increased dipole lengths (Günther, 2004) by injecting current between adjacent odd numbers (1-3, 3-5 etc.) and every fourth electrode (1-5, 5-9, etc.). The remote units were configured such that the potential dipole length equals the current dipole length. In total, a number

of 61 current injections was done.

To carry out a statistical time series analysis the instrument separates the time series into sections (partitions) of identical length. Depending on  $f$  we used between 6 (low  $f$ ) and 30 partitions (high  $f$ ), which can be considered as stacks. The number of samples per partition varies between 20 and 160. The 14 frequencies took together about 4 minutes per current dipole such that the total measuring time for the whole profile was about 4.5 hours. For using even lower frequencies, the measuring time increases rapidly. Although signal-to-noise ratio improved towards lower frequencies and the number of partitions can be reduced, the measuring time is expected to almost double for every lower frequency step.

[Figure 2 about here.]

Figure 2 shows an example spectrum for the current injection into the electrodes 1 and 3. The individual readings with a dipole length of  $a=2$  m and separation factors of  $n=1-9$  represent deeper penetration depths averaging over a wider range along the profile. The apparent resistivities (top) show almost linear decrease (log-log plot), only the shallowest measurement is a bit smaller ( $130 \Omega\text{m}$ ) than the others ( $\approx 200 \Omega\text{m}$ ).

The phases show a Cole-Cole type behaviour with very low peak frequencies at about 0.1 Hz that are sometimes not even reached by the measured frequency range. For two dipoles we see another peak at high frequencies for which it is hard to decide whether the origin is induced polarisation, capacitive coupling between cables or a high-frequency dielectric effect (Florsch



et al., 2014) as all of the effects show similar behaviour and dominate at low signal strength. The maximum phase values are in general very high and increase from about 100 mrad for the shallowest measurements to about 270 mrad at a separation level of  $n=7$  before they start to decrease again. In comparison, Florsch et al. (2011) reported phase values of up to 80 mrad in the field and 170 mrad in the laboratory.

↑ 3-3

The errors bars, based on the statistical time series analysis of the partitions indicate a very good data quality with only a few exceptions at 1.25 Hz and 40 Hz. The spectra of the other dipoles show similar behaviour. In some measurements there are single outliers (not shown) that are to be removed by hand or a robust algorithm.

As the current flowing to the current electrodes induces voltages at the passed voltage dipoles, we used only potential dipoles ahead of the current dipole. Furthermore we deleted all measurements with geometric factors above a value of 50,000 m since those are associated with very low voltage gains and higher errors. Finally, we ended up in a number of about 750 data points per frequency.

[Figure 3 about here.]

Figure 3 shows the pseudosection of apparent resistivities (top) and phases (bottom) for the lowest frequency corresponding to the observed phase maximum in Fig. 2. Both images exhibit only smooth changes and indicate excellent data quality. The minimum resistivity of about  $100 \Omega\text{m}$  is found at the top. Below, there is a clear separation between left ( $\approx 200 \Omega\text{m}$ ) and right

( $\approx 300\text{-}400\ \Omega\text{m}$ ). The apparent phases are very low at the top and increase with higher penetration depth. The highest values of more than 250 mrad are found in the left and right at medium separations and indicate the strongly polarisable body of slag material. Before inverting these data, we build a synthetic model based on the raw data observations to test the inversion algorithms.

### 3. Synthetic modelling

In order to do systematic tests on a known model, we make use of a synthetic model consisting of an outcropping slag body below an overburden and above a bedrock. Figure 1 shows the discretization of the four regions.

[Figure 4 about here.]

All regions are assumed to show Cole-Cole behaviour (eq. 7), see Table 1 for their parameters. The resistivities are quite similar in a range of a few hundred  $\Omega\text{m}$ . The bedrock itself is rather resistive and non-polarisable like the rather conducting topsoil. The highly polarisable ( $m=0.7/0.8$ ) slag heap is divided into two parts (slag1/2) with differing time constants ( $\tau=0.1$  and 1 s).

[Table 1 about here.]

The questions to be answered are:

- Can we image the correct slag shape from single or multiple frequencies?

- Do different frequencies distinguish the slag bodies?
- Can we recover the spectral parameters  $m$  and  $\tau$ ?

The same dipole-dipole electrode array as measured in the field case is used for the simulations. Following Kemna (2000), a complex forward calculation for every frequency is done to generate the synthetic data.

[Figure 5 about here.]

Figure 5 shows the noise-free synthetic data for two example frequencies. The resulting apparent resistivities look similar and show the expected  $100\ \Omega\text{m}$  at the surface and increased values above  $200\ \Omega\text{m}$  for deeper penetration depths. The values for the higher frequency are lower due to the subsurface chargeabilities. The phases show quite different anomalies reaching values of about  $250\ \text{mrad}$ : For  $f=312\ \Omega\text{m}$  we see mainly the anomaly on the right-hand side associated with slag2 that has a high time constant. The higher frequency shows two anomalies. The one of the right-hand side is diminished and on the left-hand side dominates the effect of slag1 exhibiting a lower time constant.

The data were contaminated by Gaussian noise using standard deviations of 2% (relative error) and  $5\ \text{mrad}$  (absolute error) for amplitude and phase, respectively. Figure 6 shows the retrieved amplitude and phase distributions for all frequencies.

[Figure 6 about here.]

The resistivity images are not changing much along frequency and show a good conductor over a resistor. All values decrease steadily with frequency. In contrast, the phases are more interesting. For low frequencies, slag 2 shows values of up to 200 mrad. As we go to higher frequencies, the phases decrease, whereas for slag 1 they increase and fade out towards the highest frequencies. To assess the spectral recovery, we chose some points within the two slag bodies and extracted the values of the containing cells.

[Figure 7 about here.]

Figure 7 shows resistivity and phase spectra for these cells. Resistivities start at  $200 \Omega\text{m}$  and  $150 \Omega\text{m}$  for slag 1 and slag 2, respectively, and decrease with frequency. However, even though resistivity was spectrally constrained, the values are still varying. This is probably a result of the very low gradients in the synthetic model in conjunction with the noise. In contrast, the phases show a smooth spectral behaviour due to their large values and strong contrasts. The curves show a clear Cole-Cole type behaviour and were fitted for each model cells as done in TD by Yuval & Oldenburg (1997). The results are given in the legend of Fig. 7 are quite close to the synthetic values.

The fitting was done for all model cells. Figure 8 shows the distribution of the Cole-Cole parameters. Resistivity is left out as it resembles amplitude for the lowest frequency. The chargeability  $m$  clearly delineates the whole slag heap, particularly vertically, however there are some artifacts towards the boundary and below the slag. The slag parts cannot be distinguished by  $m$ , but by clearly by the time constant  $\tau$  that reproduces the synthetics. However, the

$\tau$  distribution is smeared to below as there is no information on it in regions of vanishing  $m$ . The exponent  $c$  is expected to exhibit least resolution and shows therefore a quite smooth distribution. The slag is associated with high values just below the synthetic value of 0.5, whereas the rest of the subsurface stays at the starting value of 0.25.

[Figure 8 about here.]

#### 4. Inversion of field data

First, a single-frequency inversion of the lowest measuring frequency is done. Figure 9 shows the retrieved resistivity and phase sections.

[Figure 9 about here.]

Resistivity shows roughly a three-layer behaviour. On top a homogeneous, 1 m thick layer, of about  $100 \Omega\text{m}$  can be interpreted as overburden or soil layer. Below, a high resistivity zone ( $\approx 500 \Omega\text{m}$ ) is observed whose thickness increases from the middle of the profile. These could be attributed to dry rocks or gravelly sediments. At a depth of about 3-4 m, the water level of the adjacent river, we found lower resistivities in the range of  $100\text{-}200 \Omega\text{m}$ . Looking at the phase shifts, we also find a predominantly layered behaviour, but with larger variations. On top there is a non-polarisable zone whose thickness is larger than the first resistivity and increases from the middle of the profile on. Below, we clearly see a thin, highly polarisable, zone that can clearly be attributed to slag with high mineral content. In the left part it

coincides with the high resistivity, but in the right part is present only at the lower boundary of the resistive zone. Below, we see mainly impolarisable material with an exception at about 10 m, where a high polarisation occurs at depth. However, the origin of this anomaly is not clear and could be a 3D effect, i.e. higher polarisable material at the surface besides the profile. As the next step, we do the same procedure for the highest measured frequency (1 kHz). The resistivity looks very similar but with lower amplitudes in the middle. Therefore we compute a chargeability after eq. (3). It is shown along with the phase in Figure 10.

[Figure 10 about here.]

The chargeability shows a polarisable zone with values of about 0.7 in form of a relatively thick layer. Reason for this widening might be a decreased resolution of the high frequency data due to EM coupling. The phase inversion looks generally similar as for low frequency, but with lower anomaly. Furthermore it bears more small structured anomalies that are likely artefacts. On the left-hand side, the main zones coincide very well between the two frequencies. In the right-hand side, the high phases are located much shallower. This could be due to varying material with different frequency peaks. In this case, the resulting time constants would indicate a variation in grain size or fluid conductivity. The same procedure, i.e. independent inversion, is repeated for all frequencies. Next, we do a simultaneous constrained inversion of all frequencies. In both cases we strived for a comparable chi-square data misfit of about 1.0 using a relative error of 2% and a voltage error of

$10 \mu\text{V}$  for the resistivities and an absolute error of 3 mrad for the phases. The results are summarized in Figure 11.

[Figure 11 about here.]

In order to compare the results, we pick three cells for which the retrieved resistivity amplitudes and phases are extracted. The positions to be chosen are (A) in the middle of the left anomaly (12 m, -2 m), (B) at the top (23 m, -1.5 m) and (C) at the bottom (23 m, -3.5 m) of the right anomaly. Figure 12 compares the model spectra for the cells whose midpoint is closest to the chosen point.

[Figure 12 about here.]

The resistivity spectra are very flat for both inversion techniques, particularly for point A. However, there are significant differences for point B and slight differences for point C. All curves can be fit by Cole-Cole curves (solid and dashed lines). The phase spectra look very different for the two inversion methods. The phases of the individual inversion show oscillations between the neighbouring frequencies. To the contrary, the frequencies of the simultaneous inversions are much better aligned to each other and can nicely fitted by Cole-Cole curves. Note that here the highest three frequencies were not used by the fit as the data quality is significantly worse.

Table 2 shows the retrieved parameters from fitting the amplitudes and phases.  $m$  can reliably determined by both spectra and is in the range of 0.7

or even above. To the contrary, the time constants are very different. Obviously the smoothing of the amplitudes along the frequency axis moves the sharpest gradients from the boundary to the interior thus leading to too low  $\tau$  that are better determined from the phases. The exponent  $c$  does not add much information: as in the synthetic model it exhibits values of about 0.5.

[Table 2 about here.]

Like these examples, all model cells were fitted automatically. Figure 13 shows the distribution of the chargeability and time constant for the whole subsurface. As in Fig. 10, the chargeability reaches values of about 0.7 in the slag body. The structure however is not as thick as deduced from the frequency effect of pure dc inversions, which are more prone to ambiguity. To the contrary, the region of large time constants (about 1-3 s) corresponding to the low-frequency effects is much deeper. It is not clear whether this is due to presence of less concentrated slag material or merely an inversion artifact.

[Figure 13 about here.]

## 5. Discussion

Simulations with the synthetic model show that both amplitude and phase can be reconstructed for the individual frequencies. The proposed algorithms, independent and simultaneous inversion, generally suit to reconstruct both amplitude and phase anomalies within typical ambiguity. The imaging performance depends a lot on data quality, but also on the present parameter



contrasts; in our synthetic model the resistivity contrasts are too weak for further analysis. Spectral information is retrieved by extracting the values for the individual frequencies from the model cells. Note that there is no smoothing or interpolation applied as we use the same mesh for all frequencies. At least for the well-resolved part of the subsurface with significant polarisation both chargeability and time constant can be retrieved, also the exponent provided reliable values.

The simultaneous inversion produces significantly smoother spectra that can more accurately be fitted. In case of sufficiently strong polarisation effects in the observed frequency range one can use the amplitudes not only for determining the chargeability (the classic method used in IP surveying) but also the time constant. However, the latter is more accurately determined from the phase spectra. The synthetic model demonstrates that despite existing inversion artefacts the conjunction of  $m$  and  $\tau$  is able to delineate the slag body correctly, but also to distinguish different parts.

If one tries to fit amplitude and phase at the same time it can be observed that both are not perfectly fitting together. The Kramers-Kronig relations, by which imaginary parts can be computed from real part and vice versa, indicate that there are model inconsistencies caused by inversion artifacts. A way out is an intrinsic parameterization of the subsurface, e.g. by inverting directly for Cole-Cole parameters, which is expected to work well for the presented field case but not in general. Note that our inversion approach is more flexible as it does not require a specific behaviour, but only sufficient smoothness that is guaranteed by all models. The Cole-Cole model

introduces additional non-linearity to the inversion and worsens the ill-posed inverse problem (Florsch et al., 2014). Consequently the result of such an inversion will strongly depend on the starting model. A simultaneous inversion with subsequent Cole-Cole fit as we presented can generate a starting model which is sufficiently close to the solution. This strategy of smooth inversion ahead of block inversion is actually a popular and robust technique for other inversion tasks. Another way would be a model reduction by clustering model cells and a subsequent optimization of the spectral parameters only. If the subsurface shows more complicated spectra, one could use multiple Cole-Cole terms or a smooth distribution of spectral chargeabilities using continuous Debye or Warburg models (Florsch et al., 2014).

↑ 1-1

The quality of results depends on the data quality, which is expected to be frequency-dependent, i.e. phases will have increased noise levels for higher frequencies. Independent on the used approach, we account for differing data quality by error-weighting. However, a good procedure for reciprocal data analysis (Orozeo et al., 2012b) is needed that requires measuring the profile from the other side. For the presented field data, data is of excellent quality due to the strong signals and good conditions. Hence we can clearly estimate the spatial extent of the slag material. A rather dense number of profiles would be needed to estimate the total volume of the slag body. However, to substantiate economic evaluation of possible re-exploitation further quantities are needed. Laboratory investigations (Hupfer et al., in press) give valuable information on how to use the spectral parameters. First, the determined chargeabilities of  $m=0.7$  indicate ore concentrations of about 10%.

Moreover, the normalized time constant  $\tau/\rho$  shows the best correlation to grain size with least dependence from pore water fluid. Using the fitted values of Tab. 2 we obtain values of about  $5\text{e-}3\text{s}/\Omega\text{m}$  which are associated with grain sizes of about 1 cm if the Galenite equation is used. This agrees roughly with first samples from the field.

However there are a few issues that hinder the direct translation from the laboratory into the field. First, in the field we do not have full saturation as in the lab which motivates measurements under partly saturated conditions. Next, a detailed analysis of the mineralogy and comparative probe measurements needs to be done. Then we have usually a limited frequency range in the field, i.e. exclude low  $f$  facing extensive measuring time and high values due to EM coupling. Also, temperature could play an important role (e.g., Binley et al., 2010).

## 6. Conclusions

Spectral induced polarization is a very useful technique for investigating slag heaps or mining tailings, since the anomalies are very strong. The use of a broad frequency range enables characterizing the strength and spectral behaviour of the polarisation in the subsurface assuming appropriate inversion methods. The presented simultaneous inversion of all data with smoothness constraints along the frequency axis proved to be an effective and general method that does not assume a special behaviour. Spectral parameters can be retrieved from the inverted spectra and give valuable information on mineral content and grain size assuming complementary laboratory mea-

surements are done. Further improvements could be a direct inversion for Cole-Cole parameters or a smooth Debye or Warburg model parameterisation. Spectral investigations and associated analysis tools are also expected to be a useful tool for other targets, e.g. for environmental or hydrogeological investigations.

## 7. Acknowledgment

The project ROBEHA was funded by the Germany Ministry of Education and Research (BMBF) in the framework of FONA - Research for Sustainable Development, ( $r^3$  - Innovative Technologien für Ressourceneffizienz Strategische Metalle und Mineralien) under grant 033R105. We thank Dr. Carsten Rücker (TU Berlin) for his help implementing the complex forward calculation and Kerstin Kuhn (BGR Hannover) for the mineralogical background.

## References

- Attwa, M., Günther, T., Grinat, M., & Binot, F. (2011). Evaluation of DC, FDEM and IP resistivity methods for imaging perched saltwater and a shallow channel within coastal tidal flat sediments. *Journal of Applied Geophysics*, *75*, 656–670.
- Beard, L. P., Hohmann, G. W., & Tripp, A. C. (1996). Fast resistivity/IP inversion using a low-contrast approximation. *Geophysics*, *61*, 169–179.
- Binley, A., Kruschwitz, S., Lesmes, D., & Kettridge, N. (2010). Exploiting

- the temperature effects on low frequency electrical spectra of sandstone: A comparison of effective diffusion path lengths. *Geophysics*, 75, A43–A46.
- Coggon, J. (1973). A Comparison of IP Electrode Arrays. *Geophysics*, 38, 737–761.
- Dahlin, T., & Leroux, V. (2012). Improvement in time-domain induced polarization data quality with multi-electrode systems by separating current and potential cables. *Near Surface Geophysics*, 10, 545–565. doi:10.3997/1873-0604.2012028.
- Fiandaca, G., Ramm, J., Binley, A., Gazoty, A., Christiansen, A. V., & Auken, E. (2013). Resolving spectral information from time domain induced polarization data through 2-D inversion. *Geophysical Journal International*, 192, 631–646. doi:10.1093/gji/ggs060.
- Florsch, N., Llubes, M., Téreygeol, F., Ghorbani, A. & Roblet, P. (2011). Quantification of slag heap volumes and masses through the use of induced polarization: application to the Castel-Minier site. *Journal of Archaeological Science*, 38, 438–451. doi:10.1016/j.jas.2010.09.027.
- Florsch, N., Llubes, M., & Téreygeol, F. (2012). Induced polarization 3D tomography of an archaeological direct reduction slag heap. *Near Surface Geophysics*, 10, 567–574. doi:10.3997/1873-0604.2012042.
- Florsch, N., Revil, A., & Camerlynck, C. (2014). Inversion of generalized relaxation time distributions with optimized damping parameter. *Journal*

- of *Applied Geophysics*, 109, 119–132. doi:10.1016/j.jappgeo.2014.07.013.
- Günther, T. (2004). *Inversion Methods and Resolution Analysis for the 2D/3D Reconstruction of Resistivity Structures from DC Measurements*. Ph.D. thesis University of Mining and Technology Freiberg. Available at <http://nbn-resolving.de/urn:nbn:de:swb:105-4152277>.
- Günther, T., & Rücker, C. (2005-2015). *Boundless Electrical Resistivity Tomography (BERT) – User Tutorial*. URL: <http://www.resistivity.net>.
- Günther, T., Rücker, C., & Spitzer, K. (2006). Three-dimensional modeling and inversion of DC resistivity data incorporating topography - Part II: Inversion. *Geophys. J. Int.*, 166, 506–517. doi:10.1111/j.1365-246X.2006.03011.x.
- Hönig, M., & Tezkan, B. (2007). 1D and 2D Cole-Cole-inversion of time-domain induced-polarization data. *Geophys Prospect*, 55, 117–133. doi:10.1111/j.1365-2478.2006.00570.x.
- Hördt, A., Blaschek, R., Kemna, A., & Zisser, N. (2007). Hydraulic conductivity estimation from induced polarisation data at the field scale – the Krauthausen case history. *J. Appl. Geophys.*, 62, 33–46.
- Hupfer, S., Martin, T., Weller, A., Kuhn, K., Gnther, T., Ngninjio, V., & Noell, U. (in press). Laboratory SIP measurements at unconsolidated sulphide-sand-mixtures. *Journal of Applied Geophysics*, In press.

- Ingeman-Nielsen, T., & Baumgartner, F. (2006). Numerical modelling of complex resistivity effects on a homogenous half-space at low frequencies. *Geophysical Prospection*, 54, 261–271.
- Karaoulis, M., Revil, A., Tsourlos, P., Werkema, D., & Minsley, B. (2013a). IP4DI: A software for time-lapse 2D/3D DC-resistivity and induced polarization tomography. *Computers & Geosciences*, 54, 164–170.
- Karaoulis, M., Tsourlos, P., Kim, J.-H., & Revil, A. (2013b). 4D time-lapse ERT inversion: introducing combined time andspace constraints. *Near Surface Geophysics*, 12, 25–34.
- Kemna, A. (2000). *Tomographic inversion of complex resistivity*. Ph.D. thesis Ruhr-Universität Bochum.
- Kemna, A., Binley, A., Cassiani, G., Niederleithinger, E., Revil, A., Slater, L., Williams, K. H., Orozco, A. F., Haegel, F.-H., Andreas Hrdt and, S. K., Leroux, V., Titov, K., & Zimmermann, E. (2012). An overview of the spectral induced polarization method for near-surface applications. *Near Surface Geophysics*, 10, 453–468. doi:10.3997/1873-0604.2012027.
- Kemna, A., Binley, A., & Slater, L. (2004). Crosshole IP imaging for engineering and environmental applications. *Geophysics*, 69, 97–107.
- Kim, J.-H., Yi, M., Park, S., & Kim, J. (2009). 4-D inversion of DC resistivity monitoring data acquired over a dynamically changing earth model. *Journal of Applied Geophysics*, 68, 522–532.

- Lesmes, D., & Frye, K. (2001). Influence of pore fluid chemistry on the complex conductivity and induced polarization responses of Berea sandstone. *Journal of Geophysical Research*, *106*, 4079–4090.
- Loke, M., Chambers, J., & Ogilvy, R. (2006). Inversion of 2D spectral induced polarization imaging data. *Geophys. Prospect.*, *54*, 287–301.
- Marshall, D., & Madden, T. (1959). Induced polarisation, a study of its causes. *Geophysics*, *24*, 790–816.
- Martin, T., & Günther, T. (2013). Complex resistivity tomography (CRT) for fungus detection on standing oak trees. *European Journal of Forest Research*, *132*, 765–776. doi:10.1007/s10342-013-0711-4.
- Oldenburg, D. W., & Li, Y. (1994). Inversion of induced polarization data. *Geophysics*, *59*, 1327–1341.
- Orozco, A. F., Kemna, A., Oberdörster, C., Zschornack, L., Leven, C., Dietrich, P., & Weiss, H. (2012a). Delineation of subsurface hydrocarbon contamination at a former hydrogenation plant using spectral induced polarization imaging. *Journal of Contaminant Hydrology*, *136–137*, 131–144. doi:10.1016/j.jconhyd.2012.06.001.
- Orozco, A. F., Kemna, A., & Zimmermann, E. (2012b). Data error quantification in spectral induced polarization imaging. *Geophysics*, *77*, E227–E237. doi:10.1190/geo2010-0194.1.



- Pelton, W., Rijo, L., & C.M. Swift, J. (1978a). Inversion of two-dimensional resistivity and induced-polarization data. *Geophysics*, 43, 788–803.
- Pelton, W., Ward, S., Hallof, P., Sill, W., & Nelson, P. (1978b). Mineral discrimination and removal of inductive coupling with multifrequency IP. *Geophysics*, 43, 588–609.
- Poggendorf, C., Rüpk, A., Gock, E., Sahel, H., Kuhn, K., & Martin, T. (2015). Nutzung des Rohstoffpotentials von Bergbau- und Hüttenhalden am Beispiel des Westharzes. In K. J. Thome-Kozmiensky (Ed.), *Mineralische Nebenprodukte und Abfälle 2 Aschen, Schlacken, Stäube und Baurestmassen*. TK Verlag, Neuruppin. (in German).
- Radic, T. (2004). *SIP256C - Users manual*. Radic Research [www.radic-research.de](http://www.radic-research.de).
- Routh, P. S., & Oldenburg, D. W. (2001). Electromagnetic coupling in frequency-domain induced polarization data: a method for removal. *Geophys. J. Int.*, 145, 59–76. doi:10.1111/j.1365-246X.2001.00384.x.
- Routh, P. S., Oldenburg, D. W., & Li, Y. (1998). Regularized inversion of spectral IP parameters from complex resistivity data. In *SEG Technical Program Expanded Abstracts 1998*. Society of Exploration Geophysicists. doi:10.1190/1.1820608.
- Rücker, C. (2011). *Advanced Electrical Resistivity Modelling and Inversion using Unstructured Discretization*. Ph.D. thesis University of Leipzig.

- Rücker, C., & Günther, T. (2010-2015). *Geophysical Modelling and Inversion Library GIMLi - a C++/Python Library for geophysical data analysis*. URL: <http://www.pygimli.org>.
- Rücker, C., Günther, T., & Spitzer, K. (2006). Three-dimensional modeling and inversion of DC resistivity data incorporating topography - Part I: Modeling. *Geophys. J. Int.*, 166, 495–505. doi:10.1111/j.1365-246X.2006.03010.x.
- Schmutz, M., Ghorbani, A., Vaudelet, P., & Blondel, A. (2014). Cable arrangement to reduce electromagnetic coupling effects in spectral-induced polarization studies. *Geophysics*, 79, A1–A5. doi:10.1190/geo2013-0301.1.
- Shewchuk, J. R. (1996). Triangle: Engineering a 2D Quality Mesh Generator and Delaunay Triangulator. In M. C. Lin, & D. Manocha (Eds.), *Applied Computational Geometry: Towards Geometric Engineering* (pp. 203–222). Springer-Verlag volume 1148 of *Lecture Notes in Computer Science*. From the First ACM Workshop on Applied Computational Geometry.
- Slater, L., & Lesmes, D. (2002). IP interpretation in environmental investigations. *Geophysics*, 67, 77–88.
- Udphuay, S., Günther, T., Everett, M., Warden, R., & Briaud, J.-L. (2011). Three-dimensional resistivity tomography in extreme coastal terrain amidst dense cultural signals: application to cliff stability assessment at the historic D-Day site. *Geophys. J. Int.*, 185, 201–220.

- Ullrich, B., Günther, T., & Rücker, C. (2008). Electrical resistivity tomography methods for archaeological prospection. In A. P. L. Herzog (Ed.), *Layers of Perception. Proceedings of the 35th International Conference on Computer Applications and Quantitative Methods in Archaeology (CAA), Berlin, April 26, 2007*.
- Van Voorhis, G., Nelson, P., & Drake, T. (1973). Complex resistivity spectra of porphyry copper mineralization. *Geophysics*, 38, 49–60.
- Waxman, M., & Smits, L. (1968). Electrical Conductivities in Oil-Bearing Shaly Sands. *Society of Petroleum Engineers Journal*, (pp. 107–122).
- Yuval, & Oldenburg, D. W. (1996). DC resistivity and IP methods in acid mine drainage problems: results from the Copper Cliff mine tailings impoundments. *J. Appl. Geophys.*, 34, 187–198.
- Yuval, & Oldenburg, D. W. (1997). Computation of Cole-Cole parameters from IP data. *Geophysics*, 62, 436–448. doi:10.1190/1.1444154.

## List of Figures

- 1 Photograph showing one of the slag heap profiles with slag outcrop in the background. The yellow box is the SIP256C instrument, the grey boxes are remote units connected by fibre optic cables. Two separated electrodes at each location (one for current, one for potential measurements) were used to avoid electrode polarization. . . . . 36
- 2 Exemplary apparent resistivity (top) and phase (bottom) spectrum for the current injection between electrodes 1 and 3. The legend denotes the potential electrode numbers. . . . . 37
- 3 Apparent resistivity (top) and phase (bottom) pseudosection for the lowest frequency of 156 mHz. Below the classic dipoles ( $a=1$ ) the arrays with longer ( $a=2/4$ ) dipole lengths are plotted. 38
- 4 Synthetic slag heap model, see Table 1 for the properties of the four regions. Electrodes are marked by black wedges. . . . 39
- 5 Apparent resistivity (top) and phase (bottom) for  $f=156$  mHz (left) and  $f=5$  Hz (right). . . . . 40
- 6 Resistivity (left) and phase (right) inversion result for all frequencies. . . . . 41
- 7 Inversion result spectra for selected subsurface cells along with their Cole-Cole fit. . . . . 42
- 8 Chargeability (top), time constant (middle) and relaxation exponent (bottom) obtained by fitting the inversion results for all cells. . . . . 43
- 9 Resistivity (top) and phase (bottom) inversion result for  $f=156$  mHz 44
- 10 (Frequency effect) chargeability derived from inversion results for 156 mHz and 1 kHz (top), phase (bottom) for  $f=1$  kHz. . . 45
- 11 Results from simultaneous inversion (left: resistivity, right: phase) for all frequencies. Color scale is identical to Fig. 9. . . 46
- 12 Amplitude (top) and phase (bottom) spectra of selected model cells (A-C) retrieved from individual (ind.) and simultaneous (sim.) inversion. The solid and dashed lines represent the Cole-Cole fits based on ind. and sim., respectively. . . . . 47
- 13 Distribution of chargeability (top), time constant (middle) and relaxation exponent (bottom) retrieved from fitting the simultaneous inversion results. . . . . 48



Figure 1: Photograph showing one of the slag heap profiles with slag outcrop in the background. The yellow box is the SIP256C instrument, the grey boxes are remote units connected by fibre optic cables. Two separated electrodes at each location (one for current, one for potential measurements) were used to avoid electrode polarization.

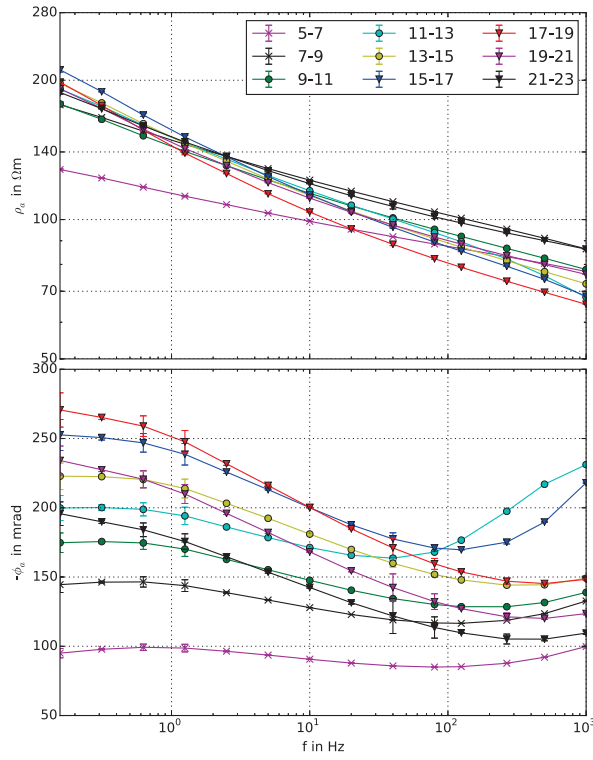


Figure 2: Exemplary apparent resistivity (top) and phase (bottom) spectrum for the current injection between electrodes 1 and 3. The legend denotes the potential electrode numbers.

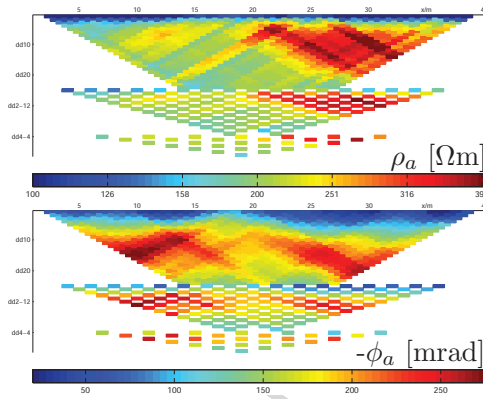


Figure 3: Apparent resistivity (top) and phase (bottom) pseudosection for the lowest frequency of 156 mHz. Below the classic dipoles ( $a=1$ ) the arrays with longer ( $a=2/4$ ) dipole lengths are plotted.

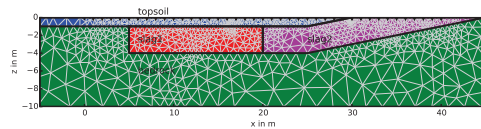


Figure 4: Synthetic slag heap model, see Table 1 for the properties of the four regions. Electrodes are marked by black wedges.



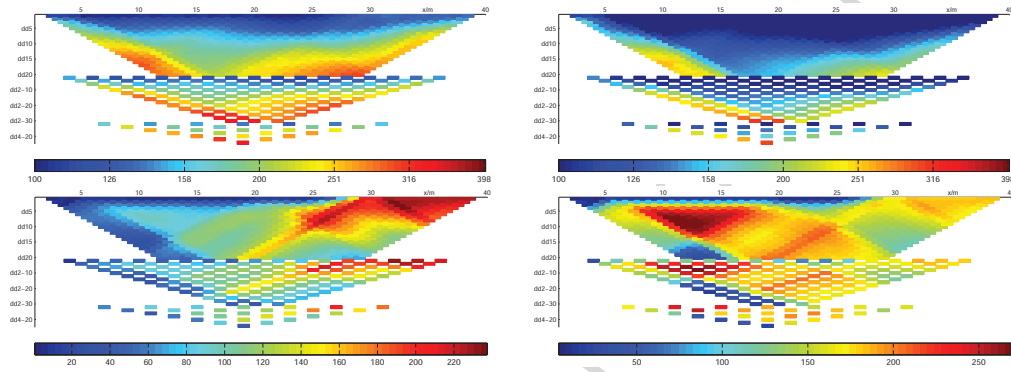


Figure 5: Apparent resistivity (top) and phase (bottom) for  $f=156$  mHz (left) and  $f=5$  Hz (right).

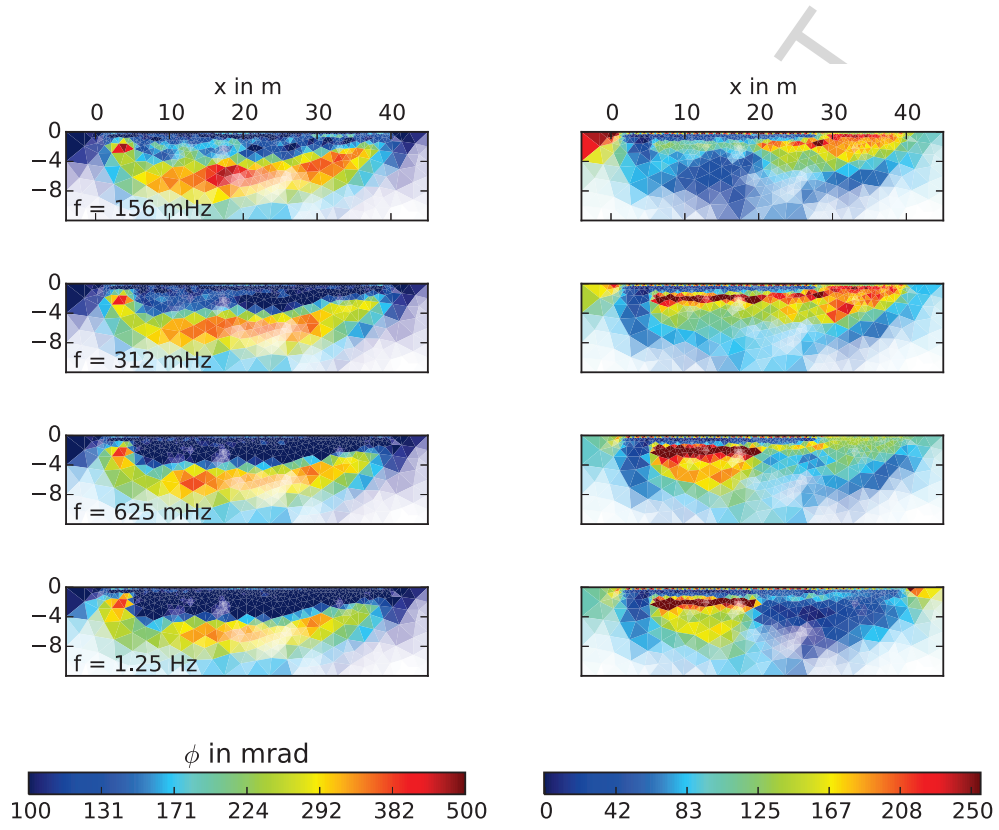


Figure 6: Resistivity (left) and phase (right) inversion result for all frequencies.

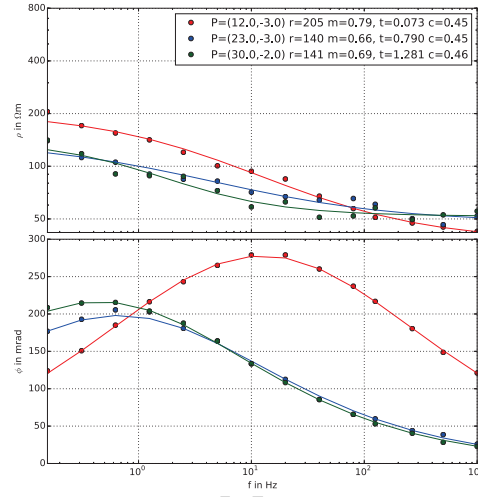


Figure 7: Inversion result spectra for selected subsurface cells along with their Cole-Cole fit.

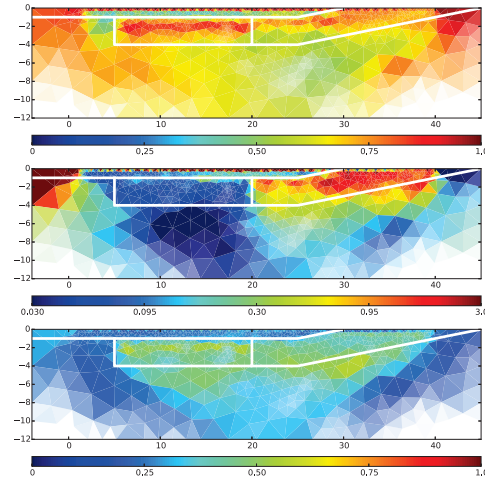


Figure 8: Chargeability (top), time constant (middle) and relaxation exponent (bottom) obtained by fitting the inversion results for all cells.

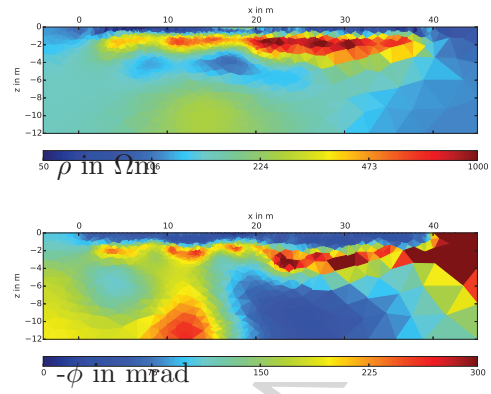


Figure 9: Resistivity (top) and phase (bottom) inversion result for  $f=156$  mHz

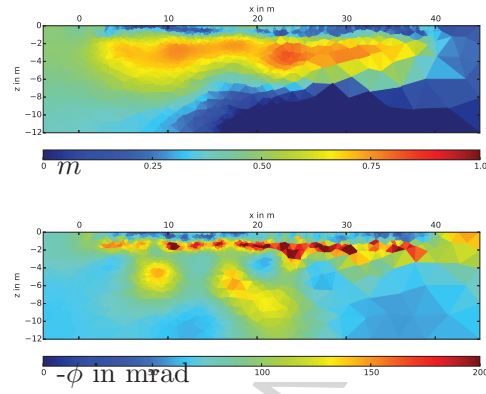


Figure 10: (Frequency effect) chargeability derived from inversion results for 156 mHz and 1 kHz (top), phase (bottom) for  $f=1$  kHz.

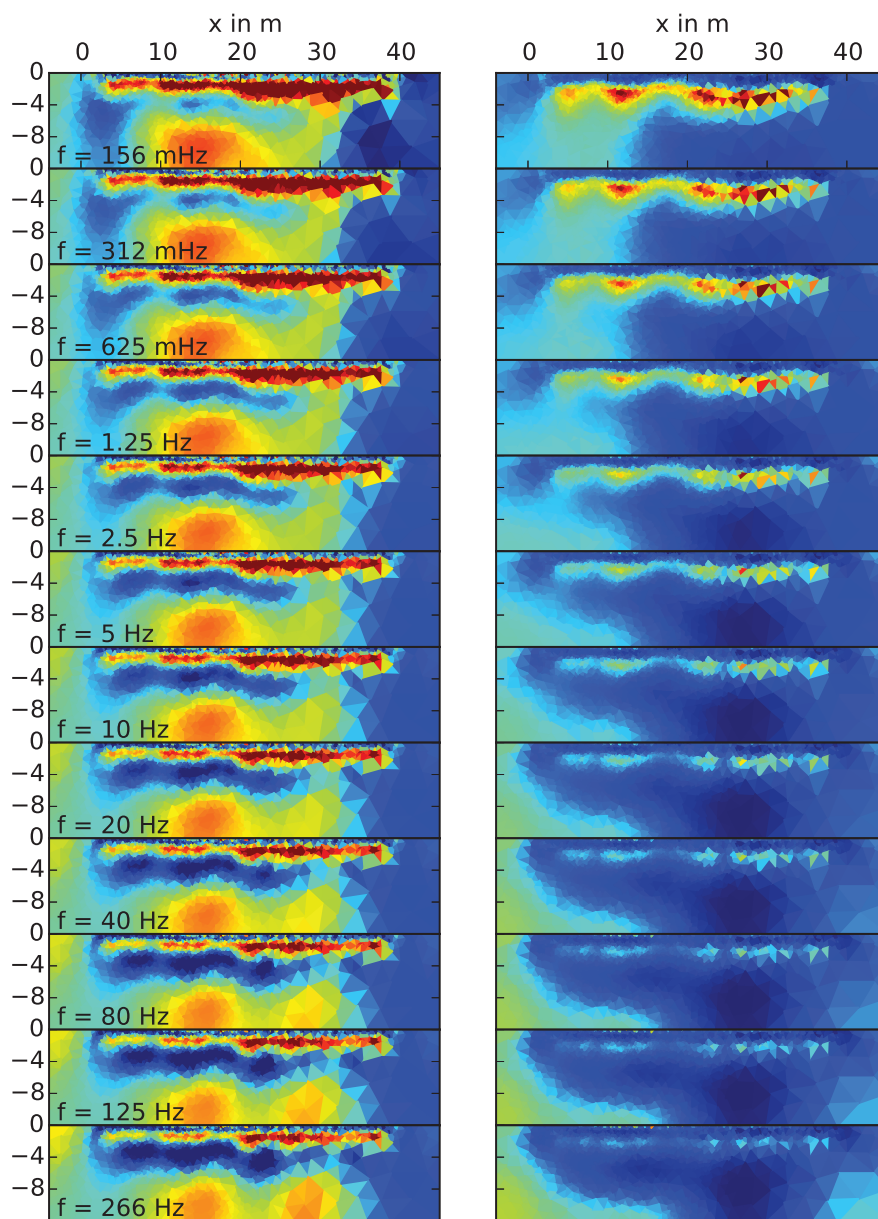


Figure 11: Results from simultaneous inversion (left: resistivity, right: phase) for all frequencies. Color scale is identical to Fig. 9.

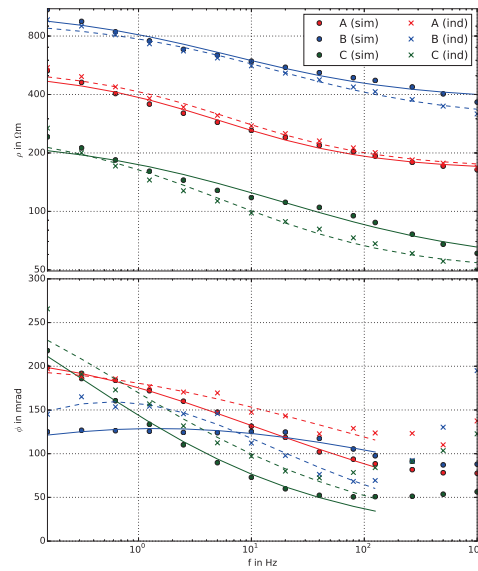


Figure 12: Amplitude (top) and phase (bottom) spectra of selected model cells (A-C) retrieved from individual (ind.) and simultaneous (sim.) inversion. The solid and dashed lines represent the Cole-Cole fits based on ind. and sim., respectively.



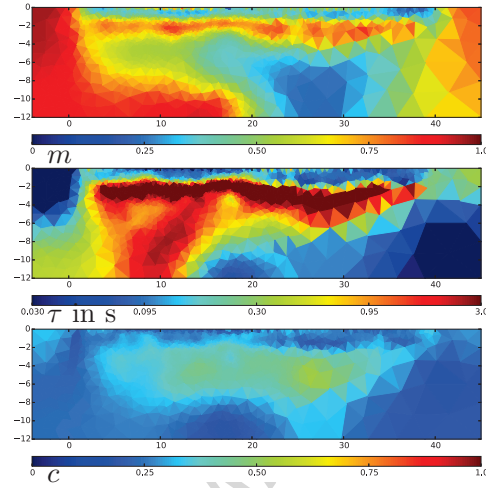


Figure 13: Distribution of chargeability (top), time constant (middle) and relaxation exponent (bottom) retrieved from fitting the simultaneous inversion results.

# **List of Tables**

- 1 Properties of the synthetic model regions: resistivity  $\rho$ , chargeability  $m$ , time constant  $\tau$  and relaxation exponent  $c$ . . . . . 50
- 2 Cole-Cole parameters for the three model points derived from amplitude ( $\rho$ ) and phase ( $\phi$ ) spectra. . . . . 51

Region	$\rho$ [ $\Omega\text{m}$ ]	$m$ [mV/V]	$\tau$ [s]	$c$ [-]
topsoil	100	0.001	0.001	0.25
bedrock	500	0.001	0.001	0.25
slag1	200	0.8	0.1	0.5
slag2	200	0.7	1.0	0.5

Table 1: Properties of the synthetic model regions: resistivity  $\rho$ , chargeability  $m$ , time constant  $\tau$  and relaxation exponent  $c$ .

		$\rho$ [ $\Omega\text{m}$ ]	$m$ [-]	$\tau$ [s]	$c$ [-]
A	sim	531	0.70	0.89	0.52
( $\rho$ )	ind	551	0.70	0.71	0.53
B	sim	696	0.35	0.15	0.69
( $\rho$ )	ind	777	0.65	0.14	0.43
C	sim	284	0.91	0.70	0.52
( $\rho$ )	ind	300	0.87	1.14	0.46
A	sim		0.79	3.72	0.32
( $\phi$ )	ind		0.84	9.71	0.27
B	sim		0.75	2.35	0.24
( $\phi$ )	ind		0.62	0.85	0.40
C	sim		0.78	4.51	0.41
( $\phi$ )	ind		0.81	5.20	0.35

Table 2: Cole-Cole parameters for the three model points derived from amplitude ( $\rho$ ) and phase ( $\phi$ ) spectra.

## Highlights

- Investigation of slag heap with SIP images slag body
- Simultaneous inversion of all data leads to interpretable subsurface spectra
- Fitting of subsurface spectra leads to chargeability and time constant distribution that can be used to derive mineral content and grain size